ADVANCED FUNCTIONAL MATERIALS
www.afm-journal.de

Textile-Based Wireless Pressure Sensor Array for Human-Interactive Sensing

Baoqing Nie, Rong Huang, Ting Yao, Yiqiu Zhang, Yihui Miao, Changrong Liu, Jian Liu, and Xinjian Chen**

A textile-based wireless pressure sensor array (WiPSA) is proposed for flexible remote tactile sensing applications. The WiPSA device is composed of a fabric spacer sandwiched by two separate layers of passive antennas and ferrite film units. Under the external pressure, the mechanical compression of the flexible fabric spacer leads to an inductance change, which can further be transduced to a detectable shift of the resonant frequency. Importantly, WiPSA integrates the ferrite film featuring an ultrahigh permeability, which effectively improves the device sensitivity and avoids the interference of conductive materials simultaneously. The device performance with a high quality factor (>35) and sensitivity (–0.19 MHz kPa^{-1}) within a pressure range of 0–20 kPa is demonstrated. In addition, WiPSA achieves excellent reproducibility under periodical pressures (>20 000 cycles), temperature fluctuations (15–103 °C), and humidity variations (40–99%). As a proof of concept for human-interactive sensing, WiPSA is successfully 1) integrated with a flexible wrist band for fingertip pressure-guided direction choices, 2) developed into a smart wireless insole to map the plantar stress distributions, and 3) embedded into a waist-supporting belt to resolve the contact pressure between the belt and human abdomen in a remote transmitting scheme.

1. Introduction

The development of electronic textiles (E-textile) is an active research area in biomedicine and robotics, which allows design of devices with a great physical flexibility, outstanding wearability, and easy integration to various fabric substrates that cannot be achieved by the traditional electronic device fabrication.[1] Textile-based pressure sensors have been proposed for a variety of applications, including wearable health monitoring, intelligent home care, medical diagnostics, and human motion detections.[2] Different sensing mechanisms based on capacitive, resistive, or piezoelectric measurements have been introduced for the development of pressure sensors in E-textile.[3] For instance, Li et al. developed a capacitive textile pressure sensor by assembly of a compliant ion-conductive polymer sandwiched between two layers of conductive fabrics to monitor pressure distributions at soft interfaces.[2c] Lee's group reported a capacitive fabric pressure sensor sewn in a glove to control quadrotor movements by detecting finger motions.[3c] However, there remain several critical issues to be addressed in this research field, including complexity of wiring, poor resilience, and signal fluctuations induced by the environmental changes, which limit the practical applications of smart E-textile devices.

Wearable electronics that exploit the technologies of wireless transmissions, such as radio frequency identification or near field communication, offers a concise platform to detect healthcare signals, including body temperature, electrophysiology, pressure, and sweat.[4] Many wireless sensors are relied on passive components, such as an inductor (L) and a capacitor (C) to transfer information in electromagnetic fields in response to external physical changes.[5] This design is featured with several intrinsic advantages, such as simplified electrical connection, no requirement for power source, long lifetime, and ease for miniaturization. Recently, a transparent soft contact lens sensor has been developed for wirelessly recording intraocular pressure. The device is built on a flexible dielectric layer sandwiched between two inductive spiral electrodes, allowing for the measurements of the intraocular pressure changes by the coupling of the capacitance and inductance.[6] Bao's group has reported a millimeter-scaled passive pressure sensor by stacking a deformable dielectric film between two inductive spiral layers, with a demonstration of in vivo intracranial pressure monitoring in mice.[7] The development of flexible wireless sensing technologies is on the urgent demand of biomedical applications, where remote detection, implantability, and robust performance are critically important.

Dr. B. Nie, R. Huang, T. Yao, Y. Miao, Dr. C. Liu, Prof. X. Chen
School of Electronic and Information Engineering
Soochow University
Suzhou, Jiangsu 215006, China
E-mail: xjchen@suda.edu.cn
Y. Zhang, Prof. J. Liu
Institute of Functional Nano and Soft Materials
Jiangsu Key Laboratory for Carbon-Based Functional Materials and Devices
Soochow University
Suzhou, Jiangsu 215123, China
E-mail: jliu@suda.edu.cn
Prof. X. Chen
State Key Laboratory of Radiation Medicine and Protection
Soochow University
Suzhou, Jiangsu 215123, China
The ORCID identification number(s) for the author(s) of this article can be found under https://doi.org/10.1002/adfm.201808786.

DOI: 10.1002/adfm.201808786

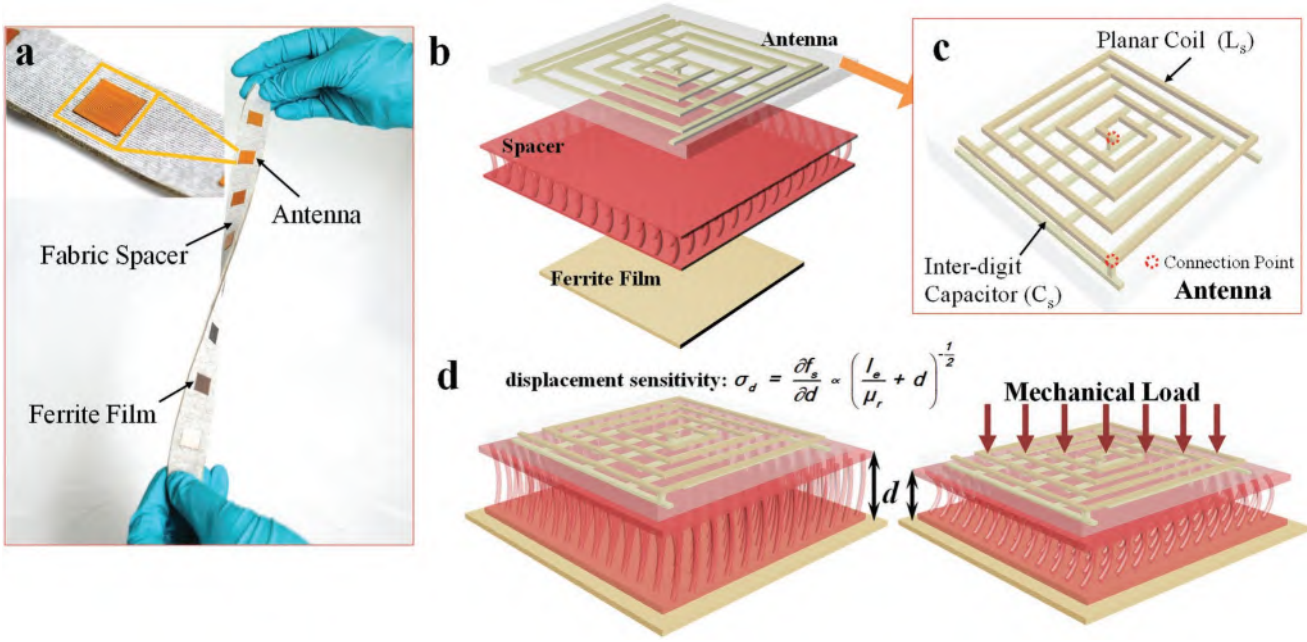

Figure 1. a) A photograph of a textile-based flexible WiPSA of 1 × 8 elements. Inset: A magnified view of one sensing unit of WiPSA. b) Schematic illustration of the 3D structure of one unit in WiPSA, consisting of a fabric spacer sandwiched between an antenna (top) and a piece of ferrite film (bottom). c) The antenna consists by a planar coil (L_s) and an interdigit capacitor (C_s), forming an LC passive resonator. The circles illustrate the connection positions of the coil and the capacitor. d) The sensor responds to an external load by mechanical deformation of the fabric spacer, resulting in a shift of the resonant frequency caused by the change of the separation distance between the ferrite film and the antenna.

Here we report a flexible, wireless pressure sensor array (WiPSA) based on E-textile technology for remote measurements of human-interactive pressure distribution at various soft interfaces. **Figure 1**a illustrates a textile-based flexible WiPSA of 1 × 8 units, of which each sensing unit comprises a layer of soft fabric spacer, sandwiched between an LC antenna and a piece of ferrite thin film. The external loads deform the flexible fabric spacer, leading to the decreases of the distance between the ferrite films and the antennas. Subsequently, the ferrite thin film promotes a dramatic change in the resonant frequencies of LC antennas. Importantly, attributing to the high permeability and radiation absorbent nature of the ferrite film, our WiPSA has been demonstrated with a device sensitivity as high as –0.19 MHz kPa^{-1} in the pressure region of 0–20 kPa, a high quality factor (QF > 35), and a great immunity to interferences of conductive materials on the resonant frequency, in comparison to the previous reports using capacitance-based methods in the literatures.[8] Our design allows an excellent signal reproducibility as the device experiences more than 20 000 cycles of external loads, accompanied by a series of tests of changing temperatures/humidity levels. WiPSA technology makes full use of the properties of the fabric material in a wireless design, promising a wide range of wearable electronic applications for contact pressure distribution measurements.

2. Results and Discussion

2.1. Operating Principle

Figure 1b exhibits the schematic illustration of a single sensing unit of WiPSA. The fabric spacer with high-density monofilament yarns separates the top passive antenna and the bottom ferrite film. Specifically, the passive antenna is designed as an inductive spiral coil (L_s) and an interdigit capacitor (C_s) connected in series, forming an LC resonator as illustrated in Figure 1c. The ferrite film assembled underneath has a high permeability and a low resistance to magnetic flux in a wide frequency range. Consequently, the effective inductance (L_e) of the device increases since the effective permeability in the surrounding environment raises. This inductance as a function of the separation distance of the ferrite film and antenna (d) can be described in the following formula[9]

$$L_e \propto \frac{\mu_r}{1 + \mu_r \times d/l_e} \tag{1}$$

where μ_r and l_e are the relative permeability and the effective magnetic path length of the ferrite membrane, respectively. According to the theoretical RLC circuit analysis, the whole structure has a unique resonant frequency (f_s) that can be expressed as

$$f_s = \frac{1}{2\pi\sqrt{L_e \times (C_s + C_p)}} \tag{2}$$

where C_p represents the parasitic capacitance, e.g., the capacitance presents between the top and bottom conductive lines. As an external load is applied, the separation distance d decreases (Figure 1d). According to Equations (1) and (2), this leads to the decrease of the resonant frequency f_s. The relationship can be simplified as

$$\frac{\partial f_s}{\partial d} \propto \frac{1}{\sqrt{l_e/\mu_r + d}} \tag{3}$$

The mechanical responses of our device are influenced by the permeability (μ_r) as well as the geometrical dimension (l_e) of the ferrite film.

2.2. Wireless Detections

The wireless detection on the resonant frequency of the sensor depends on the near-field electromagnetic communication between the sensing antenna and the external receiver. According to the well-known transformer equation, the impedance/phase loss reaches the maximum at the resonating frequency as the input power is transmitted to the resonating sensor device.[10] Here, we detect the sensor resonant frequency by searching for the maximal phase loss over the phase-frequency spectrum. The resonant frequency (f_s) of the sensor and the frequency ($f_{phase\text{-}min}$) at which the impedance phase minimum of the read antenna occurs follow the relationship

$$f_{phase\text{-}min} \approx \left(1 + \frac{1}{4}k^2 + \frac{1}{8Q^2}\right) f_s \tag{4}$$

where k is the coupling coefficient of the sensor antenna and the receiving coil and Q represents the quality factor of the sensor. Therefore, the resonant frequency is proportional to the $f_{phase\text{-}min}$ once the coupling coefficient and quality factor are constants.

Figure 2a plots the phase-frequency spectrum of the external coil when coupled to one sensing unit. As the frequency is sweeping from 30 to 55 MHz, the phase change ($\Delta\theta$) drops to a minimum value and then rebounds till it reaches the flat baseline. The $f_{phase\text{-}min}$ of 44.13 MHz is determined by locating the maximum value of the phase change ($\Delta\theta_{max} = -9.55°$) from the spectrum. In addition, the quality factor of the sensor is derived from the ratio of $f_{phase\text{-}min}$ and the −3 dB bandwidth (f_{BW}) in the phase-frequency spectrum

$$Q = \frac{f_{phase\text{-}min}}{f_{BW}} \tag{5}$$

As shown, f_{BW} is determined as 1.21 MHz, and the quality factor Q achieves 36 accordingly. Moreover, the coupling coefficient constant k is smaller than 0.66 considering the separation distance between the sensor and the read antenna is more than 4.5 mm (Equation (S1), Supporting Information). Therefore,

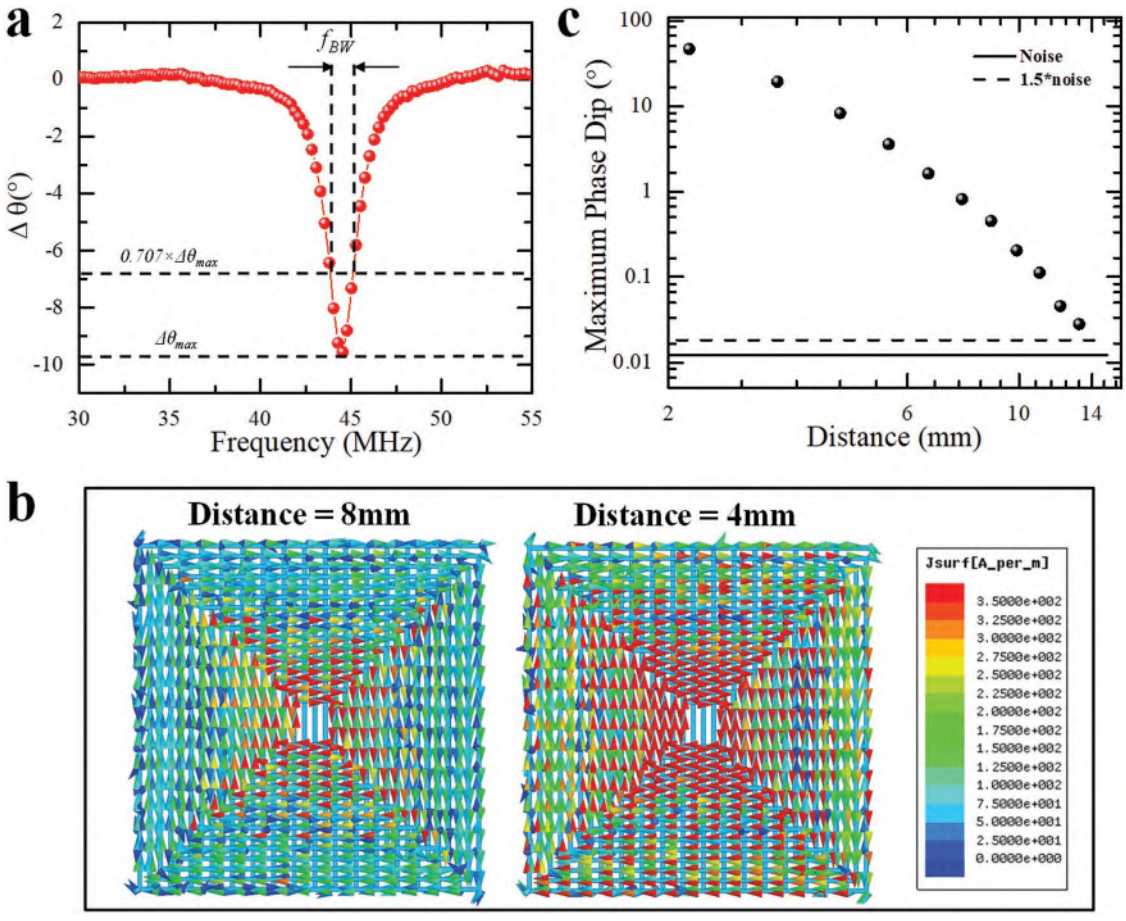

Figure 2. Experimental and computational investigations on the wireless detections of the resonant frequencies of the sensor. a) The phase changes of the read coil as a function of frequency when coupled to one WiPSA unit. b) The computational analysis on the surface current intensity in the sensor antenna as the separation distance between the antenna and the receiving coil decreases from 8 to 4 mm with an input power of 1 W. c) Experimental measurements on the maximum phase dip of the read coil as a function of the distance between the sensor and the read coil.

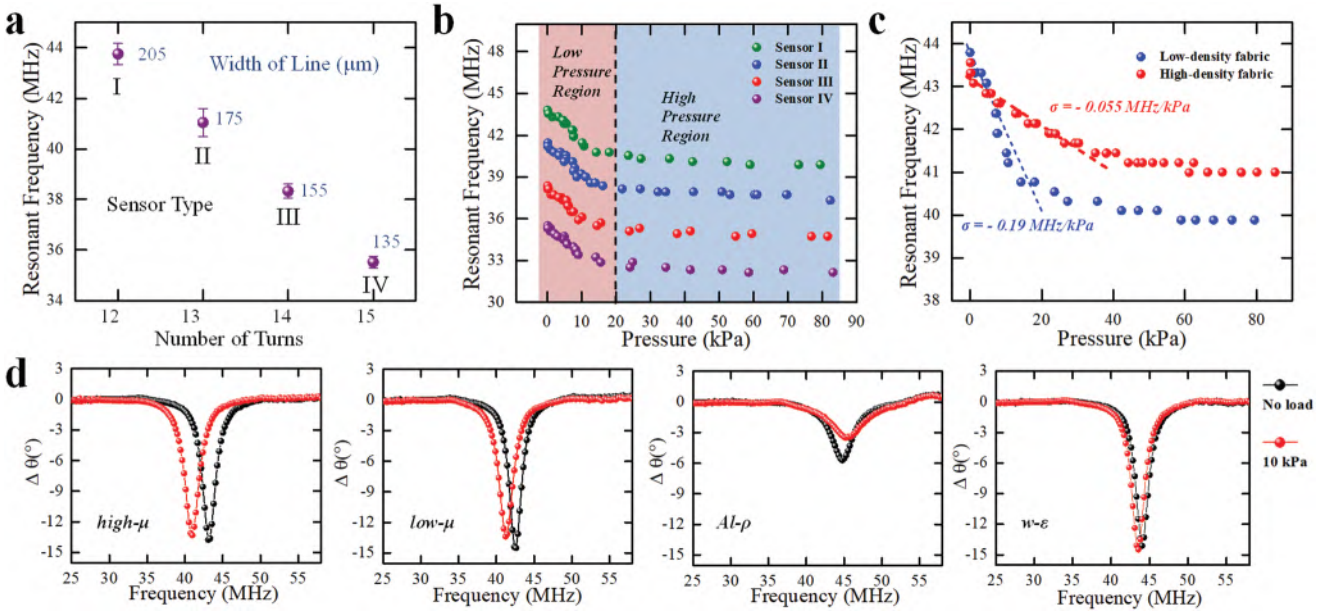

Figure 3. Characterizations on the sensor responses to mechanical loads by changing antenna design, fabric layer, and thin film material. a) The zero-pressure resonant frequency changes caused by varying the number of turns (width of line) in the antenna coil from 12 to 15 (205–135 μm), which corresponds to four types of sensors I to IV. b) Experimental investigations on the device sensitivity and dynamic range among sensors I to IV, using the same fabric spacing layer and ferrite film layer. c) Experimental investigations on the device sensitivity and dynamic range by integrating two fabric layers with different stitch density. d) Comparison on the sensor responses to an external load of 10 kPa by integrating four different film materials: a ferrite film with a high permeability (high-μ), with a low permeability (low-μ), an aluminum foil (Al-ρ), and a wet wipe (w-ε).

the resonant frequency f_s of WiPSA is approximately equal to the value of $f_{phase\text{-}min}$, considering the terms of $k^2/4$ and $1/(8Q^2)$ are much smaller than 1 in Equation (4).

The transmission distance of WiPSA is investigated by both computational analysis and experimental measurements. The surface current intensity distribution in the antenna is analyzed through a finite-element method (HFSS, Ansoft). As shown in Figure 2b, the red areas indicating a high current intensity increase sharply as the separation distance of the sensor antenna and the receiver antenna decreases (from 8 to 4 mm), implying a significant enhancement in the transmission power. In experimental validations, the maximum phase dip as a function of the separation distance between the wireless sensor and the readout antenna is presented in Figure 2c. As the separation distance decreases from 13.2 to 2.2 mm, the maximum phase dip level increases dramatically (more than 98%) because the energy gain in the near-filed transmission is linear to the second power of the transmission distance.[11] Accordingly, the maximum working distance is determined when the phase dip at the resonant frequency falls below the minimum detectable signal level.

2.3. Influences of Antenna Design on Mechanical-to-Electrical Responses

As a vital part of the sensor, the antenna design greatly influences the sensor performances, including the resonant frequency, the quality factor, the coupling coefficient, and the wireless detection distance.[12] Four types of sensors with different antennas have been fabricated by tuning the number of turns (n)/the width of line (w_l) of the antenna coils. More details for the antenna parameters are summarized in Table S1 in the Supporting Information. As shown in **Figure 3**a, the zero-pressure resonant frequencies of four types of sensors (I, II, III, and IV) are compared. As the number of turns/the width of the line is varied (12–15/205–135 μm), the corresponding resonant frequency decreases from 43.69 to 35.91 MHz. In addition, our experimental results suggest that the quality factors of the four type sensors are all above 35 (Figure S1, Supporting Information).

We have also conducted the experimental investigations on the resonant frequency responses to a broad range of pressures. Pressure-resonant frequency calibration curves for the four types of the sensors are summarized in Figure 3b. In general, there is a similar trend for all the curves that include two pressure windows: as the pressure (p) increases from 0 to 20 kPa, the resonant frequencies (f_0) drop linearly with a sensitivity (σ, defined as df_0/dp) of –0.19 MHz kPa^{-1}. As the pressure exceeds 20 kPa, the sensors exhibit a reduced sensitivity of 0.011 MHz kPa^{-1}. The resonant frequency–pressure behaviors can be predicted by the stress–strain curve of the fabric layer (Figure S2, Supporting Information). In this manner, the fabric may experience two important stages under a large range of mechanical compression.[13] In addition, as the pressure sweeps from 0 to 10 kPa, there is no cross-talking in the resonant frequency ranges for the four types of sensors, indicating that each sensor has a unique resonant frequency output available for a potential multiplexed detection within this pressure range. Our WiPSA can be implemented to detect a 2D spatial pressure distribution, from which the pressure on each sensing unit can be individually addressed with the unique resonant frequency.

It requires only a single readout coil, which tremendously simplifies the design for practical applications.

We have further investigated the influence of the fabric spacer on the device sensitivity, as the desired sensitivity can vary considerably for different applications. Figure 3c compares the resonant frequency responses of the sensors with two spacer layers with different stitch densities. Both the sensors integrate the same antenna design (type I). As shown, compared with the sensitivity of –0.19 MHz kPa^{-1} for the sensor with low-density fabric in the low-pressure region (0–20 kPa), the sensor with high-density fabric shows a reduced sensitivity of –0.055 MHz kPa^{-1} but an increased linear responsive region (0–32 kPa). It is attributed to a higher compression resistance of the fabric with a high density, where a larger stress is needed to reach the same strain level.[13a] Therefore, both the device sensitivity and the dynamic range are highly customizable by implementing different spacer fabric layers into the WiPSA device.

The device performance is evaluated to reveal the effects of different material compositions of the thin film underneath. As shown in Figure 3d, the phase-frequency spectra are compared for four different of devices, depending on the material choices of thin films: a ferrite film with high permeability (high-μ), a ferrite film with low permeability (low-μ), an aluminum foil (Al-ρ), and a wet wipes (w-ε). All of them are measured in two modes: with or without an external load of 10 kPa. The resonant frequency for the high-μ sensor exhibits a very sharp phase dip and the most sensitive response to the pressure, owing to the relatively high permeability of the materials. In contrast, the sensitivity of the low-μ sensor decreases by 33% than that of the high-μ sensor. This is consistent with the prediction by Equation (3), in which the resonant frequency change is larger in the sensor with a higher magnetic permeability as the sensors experience the same pressure load/compression distance. The maximum phase-dip values for the Al-ρ sensor further decrease nearly 58% due to the different operational mechanisms of the sensor implemented with the Al foil. As the ferrite film is used, the change of the resonant frequency depends on the variation of the surrounding effective permeability. However, as the aluminum foil is used, the operational mechanism relies on the eddy current effect, in which a closed-path current is generated as the aluminum film is placed in an electromagnetic field. This current produces a second electromagnetic field, which tends to reduce the intensity of the original one.[14] In the last scenario, the wet wipes dipped out from water is considered as a dielectric layer, which influences the overall capacitance of the sensor. As a result, the resonant frequency shifts down marginally as the load applies. Therefore, the high-μ ferrite film integration in our design is an optimal choice, given the facts of its excellent sensitivity and high signal to noise ratio.

2.4. Evaluations on the Performance Reliability

We have performed time-resolved experiments by applying three different mechanical loads (5k Pa, 10 kPa, and 20 kPa) periodically. The resonant frequencies of the sensor (type I) are recorded in a sampling frequency of 4 Hz (**Figure 4**a). For all the cycles of mechanical loads in different pressure ranges, the sensor is able to sensitively respond to the cyclic loads and return to its original value. The results suggest an excellent reproducibility of our sensor within the applied pressure ranges. Based on the analysis of the falling edge and rising edge in the periodic resonant frequency curves, the response and recovery times are estimated as 0.1 s under the external load of 5 kPa (Figure S3, Supporting Information). To investigate the mechanical reliability and robustness of our textile-based WiPSA, we have recorded the resonant frequency changes of the sensor enduring tens of thousands of press-and-release cycles, by using an electrical driven pin actuator. As shown in Figure 4b, the sensor maintains a constant resonant frequency even after 20 000 cycles of pressure loads, demonstrating the mechanical robustness and reliability of WiPSA. Figure 4c illustrates a minimum resonant frequency change in the experiment of multiple bending cycles (up to 100 times), when the WiPSA device is bended along the curvature of a cylinder with a radius varying from 23, 14 to 10 mm. The output fluctuation is within 2.5%, suggesting a highly reliable performance of the device for flexible sensing. Additionally, the change of the resonant frequency in response to a pressure of 10 kPa drops marginally when the device is bent under the radii of curvatures from infinite to 10 mm (Figure S4, Supporting Information).

2.5. Evaluations on the Environmental Influences

The potential effects of environmental parameter variations on the device performance have been investigated, including temperature/humidity changes and the interferences of surrounding conductive materials, e.g., metal blocks. Figure 4d illustrates the resonant frequency changes for the type I and type IV sensors over a temperature range from 15 to 103 °C. Both devices exhibit a slight drop by 2.4% in the resonant frequency over the whole temperature range. The resonant frequencies for the same sets of sensors have also been recorded under the humidity ranging from room condition (40%) to an elevated level (99%). As shown in Figure 4e, the resonant frequencies of the two devices only fall by 2.6% within the wide humidity variations. The slight change may be attributed to the hygroscopic nature of the antenna substrate (i.e., polyimide) and the water vapor permeability of the spacer fabric. The equivalent dielectric constant increases as the substrate and the fabric uptake additional moisture, leading to a small change of the device capacitance. Additionally, the performance of an LC-based sensor could be greatly influenced by surrounding conductive materials, such as metals.[15] To investigate the interference of metal material on our WiPSA, we have recorded the phase-frequency spectra for type I sensor with or without the ferrite film layer (FFL) by placing a metal block over the sensor surface. As shown in Figure 4f, in the control sample without FFL, the maximum phase dip ($\Delta\theta_{max}$) decreases by 29% and the resonant frequency increases by 3.6% when the metal is presented. For WiPSA with FFL, the $\Delta\theta_{max}$ and resonant frequency change by 11% and 1.3%, respectively. The differences in the performance between the two samples are highly attributed to the radiation absorbent nature of the ferrite film, in which less magnetic power flows into the metal and therefore less energy is generated due to the eddy current

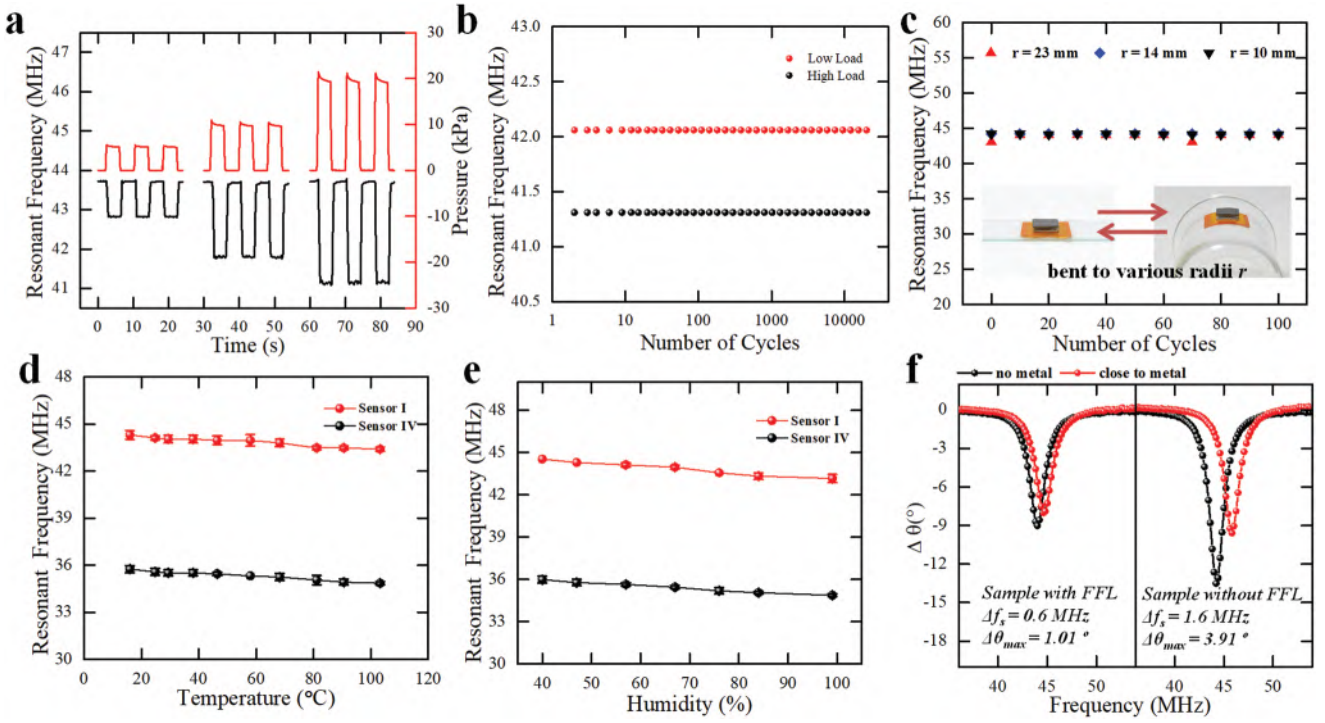

Figure 4. Characterizations on the performance reliability of WiPSA to mechanical loads and environmental influences. a) Time-resolved sensor responses under repetitive mechanical loads in the frequency of 0.125 Hz. The resonant frequency output and the pressure applied are marked as black and red curves. b) Resonant frequency measurements after repetitive cycles of external pressure (maximum cycle number >20 000). c) Resonant frequency outputs as a function of bending cycles (cylinder radius varying from 23, 14 to 10 mm). d,e) The temperature and humidity influences on the resonant frequencies for sensor type I and IV. f) Investigations on the metal influences on the resonant frequency changes (Δf_s) and maximum phase dip ($\Delta\theta_{max}$) of the samples with or without the ferrite film layer, indicating our design allows for WiPSA more robust outputs when metal materials are nearby.

effect. The outstanding stability of our WiPSA device promises wide wearable applications for human healthcare monitoring.

2.6. WiPSA for Monitoring of Human Body Movements

We have fabricated a 2 × 2 sensing array by implementing the four types of antennas (I, II, III, and IV) for the sensing units (S_d, S_r, S_l, and S_u, as marked in **Figure 5**a) and a 21 × 21 mm^2 detecting coil (right in Figure 5a). The phase-frequency spectrum of the detecting coil was recorded by placing the coil underneath the sensing array in an axial symmetry. Each unit features a unique resonant frequency within a pressure range of 0–10 kPa (Figure 5b). Therefore, both the pressure amplitude and the address of each unit in this array can be individually retrieved without any crosstalk. Figure 5c illustrates the phase dips of the detecting coil when coupled with the sensor array. The data validate the unique resonant frequencies for each unit. A smart wrist band has been developed to record the fingertip pressures by integrating our 2 × 2 textile-based WiPSA, with a demonstration of remote control of movement directions of any artificial object. The resonant frequency changes for the four units (Δf_d, Δf_r, Δf_l, and Δf_u) are recorded individually. The direction can be back calculated by considering the distribution of these variables among the sensing units of the wrist band, including $\arctan(\Delta f_u/\Delta f_l)$, $\arctan(\Delta f_d/\Delta f_r)$, $\arctan(\Delta f_d/\Delta f_l)$, and $\arctan(\Delta f_u/\Delta f_r)$. As shown in Figure 5d,e, the results of pressure mapping are distinctly differentiated in our tests of pressing on three different locations on the wrist band (Case A, Case B, and Case C). To investigate the direction controllability for the WiPSA-embedded wrist band, we have press on the S_u and S_l units randomly for 50 times (Figure S5a, Supporting Information) and the angles are summarized in Figure S5b (Supporting Information), from which the minimum detectable angle is estimated to be as sensitive as 0.5°. It is noted that the signal interference in the resonant frequency is within 0.004 MHz (equivalent to ≈21 Pa) as the sensing units are separated from each other by a distance of above 2 mm (Figure S6, Supporting Information). Therefore, the signal interferences in the resonant frequency between the four sensing units are negligible, compared with the pressure-induced frequency changes.

Plantar pressure distribution is well acknowledged for the diagnosis of foot complaints, sports biomechanics, footwear development, and gait analysis.[16] For instance, plantar pressure measurements have shown their importance in clinics for diabetic foot ulcers prevention.[17] Here, we have developed a smart wireless insole by implementing our WiPSA technology to resolve pressure distributions between the plantar surfaces and shoes. As schemed in **Figure 6**a, the pressure-sensitive insole has integrated eight of single sensing units, which are located in the positions corresponding to the areas of toe (#1), metatarsal (#2, #3), midfoot (#4 to #7), and heal (#8). The resonant frequency change for each unit was detected by placing

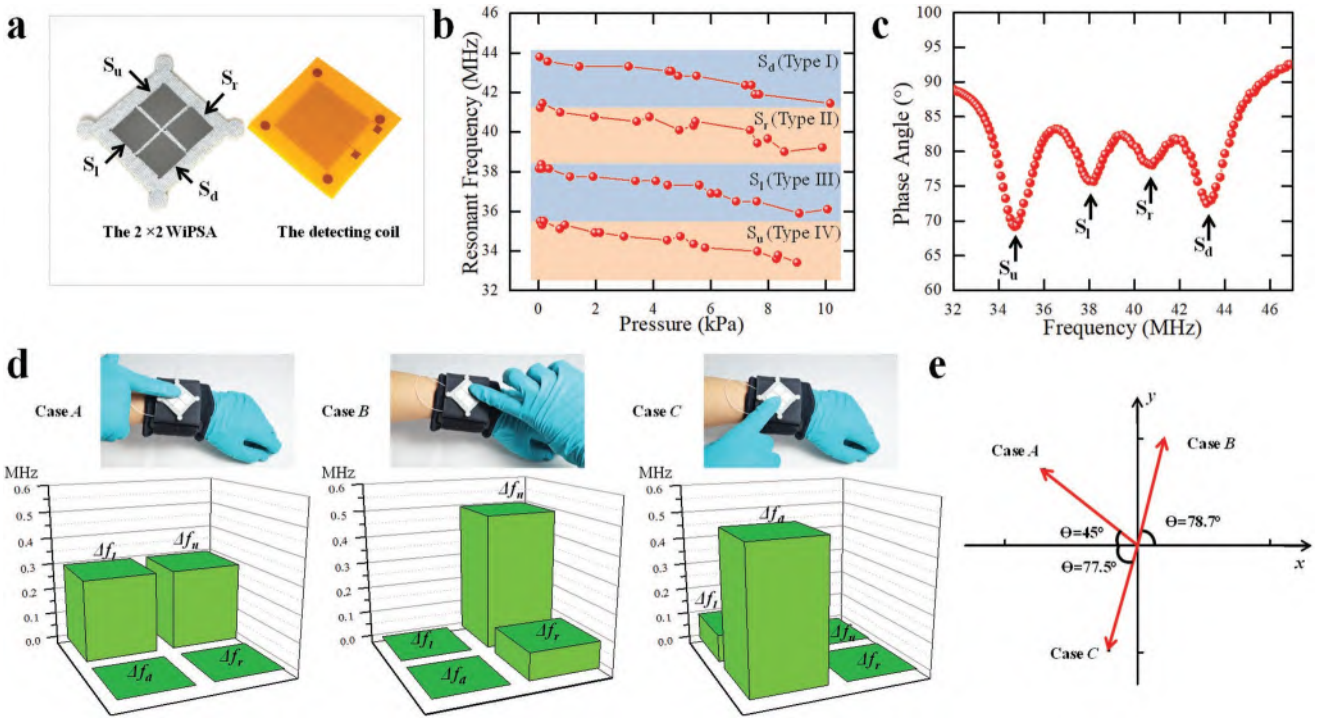

Figure 5. Application of the WiPSA device to contact pressure mapping. a) Photograph of a 2 × 2 WiPSA and a detecting coil with a surface area of 21 × 21 mm^2. b) The sensitivities of the four sensing units in the pressure range of 0–10 kPa, in which there is no crosstalk in the resonant frequency. c) The phase changes of the detecting coil as the excitation frequency sweeping from 32 to 47 MHz, in which the four distinct resonant frequencies can be detected in the phase spectrum simultaneously. d) The resonant frequency changes of the four units as the fingertip presses on three different locations (Cases A, B, and C) on a WiPSA-integrated smart wristband. e) The corresponding angles calculated from the three scenarios in (d).

a 10 × 10 mm^2 coupling coil underneath the unit coaxially. The characteristic resonant frequency–pressure responses of the eight sensors have been calibrated (Figure 6b). After a pair of smart insoles are fitted into the dancing shoes, a person of 50 kg body mass takes the footwear and stands upright or on tiptoe (insets in Figure 6c). The pressures applied by the left foot are recorded for analysis. The corresponding values for stand-upright and tiptoe gestures have been illustrated as black and red bars in Figure 6c, respectively. As expected, the foot experienced the highest stress in the heel region (sensor #8) and the lowest stress around the arch area (sensor #6) for a stand-upright posture. In contrast, for the stand-on-toe posture, the pressure levels rise in the metatarsal and toe regions and drop in the mid-foot and heal areas. Furthermore, the plantar pressure mapping has been investigated as the volunteer practices four different yoga postures (Figure 6d). The results suggest several characteristic patterns of the plantar pressure distribution along with the changes of yoga postures. For example, the pressure distributions of the left and right feet tend to be symmetrical for the posture in Figure 6d-1,d-2; in the one-leg standing posture (Figure 6d-3), the right foot holds most weight of the body and its plantar pressure values are much higher than those of the left foot; for the posture in Figure 6d-4, the right foot sustains more uniform pressure while the left foot has a higher pressure tension in the medial area.

We have further demonstrated an application for our WiPSA by integrating with a commercial waist support belt to measure the interactive pressures between the belt and a volunteer's abdomen (Figure S7a, Supporting Information). The WiPSA-embedded smart waist belt sensitively quantifies three different wrapping tensions (Figure S7c, Supporting Information). It also successfully detects the pressure differences as the volunteer takes a deep breath out and in, leading to a higher/lower stress to the belly (Figure S7d, Supporting Information). Collectively, these demonstrations with our wrist band, smart insole, and waist belt allow for sensitive and easy detection of the pressure distribution along with human body movements, offering interesting applications in the wearable healthcare system and the sports biomechanics in a wireless transmission manner.

2.7. Performance Comparison of the Wireless Pressure Sensing Technologies

Table 1 compares the performances of our WiPSA device to the state-of-the-art wireless pressure sensors. Most flexible wireless pressure sensors reported previously relies on the capacitance changes in the LC passive design, in which the capacitance values increase in response to pressures. Therefore, the effective quality factor Q is expected to degrade due to the relationship of $Q = (LC^{-1})^{1/2} \times R^{-1}$ in an LCR resonant system. In contrast, the mechanism of our WiPSA device is inductive-based pressure sensing, distinctly different from the others. The pressure-induced inductive increase ensures no quality factor Q loss in the entire sensing range. In addition, by introducing the ferrite thin film with a high permeability, our WiPSA has

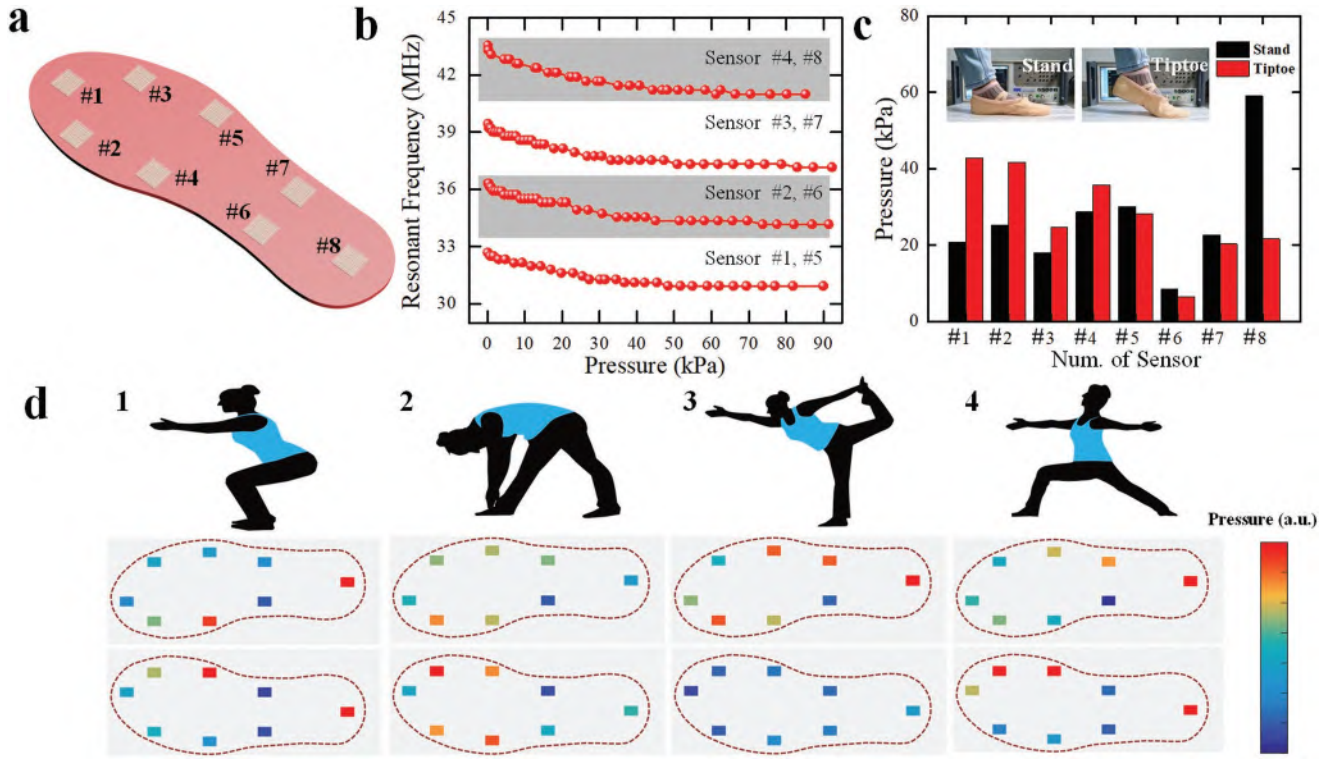

Figure 6. Demonstration of the utility of the WiPSA in plantar pressure mapping. a) An illustrative graph of a smart insole embedded with eight WiPSA units. b) Calibration on the sensitivities of the eight units within the pressure range of 0–100 kPa. c) The plantar pressure distribution of a volunteer is measured by fitting the smart insole into dance shoes. Pressure distribution differences between two gestures of stand-upright and on-tiptoe (insets) are compared. d) Four characteristic plantar distribution patterns are recorded as the volunteer changes her yoga postures.

successfully avoided the interference from metallic materials, which could be a meaningful benefit in the practically wearable applications, e.g., metal-included cell phones or watches may affect the device performance if without such an interference-free barrier. There is no similar literature report on this unique feature to our best knowledge. Furthermore, WiPSA exhibits a high effective qualify factor of ≈35, which is a critical factor in such an LC-based passive device: 1) reducing the electromagnetic energy loss for the enhanced energy storage in the system, 2) ensuring a sharp phase-dip in the phase-frequency spectrum of the read coil, to enhance the detecting accuracy of resonant frequency and reduce the overlapping area between frequency adjacent sensing units, and 3) improving in the detection distance between the sensor coil and read coil. Although our device is less sensitive than a couple of the other excellent designs in the table, it is still very competitive in comparison of the relative frequency change $df/f_0/dp$. The improvements in the future may include the materials with higher permeability or new operating designs for better performance in the device sensitivity and pressure range.

Table 1. The comparison on the device performance of wireless pressure sensing technologies.

Reference	Sensing mechanism	Dimension [mm]	Sensitivity[a] [df/dp, MHz kPa^{-1}]	Sensitivity[b] [$df/f_0/dp$, kPa^{-1}]	Quality factor	Pressure range [kPa]
[5a]	Capacitance	5 × 5 × 0.15	−2.14	-2.70×10^{-3}	25.9	0–26.7
[6]	Capacitance	Radius curvature: 14; thickness: 0.085	−19.8	-4.83×10^{-3}	Unknown	0–6.67
[7]	Capacitance	1 × 1 × 0.1	−16.91	-6.09×10^{-3}	Unknown	0–26.7
[8a]	Capacitance	Diameter: 5; needle length: 5	−0.11	-1.75×10^{-3}	26.5	0–6.67
[18]	Capacitance	4 × 1.5 × 1	−1.2	-3.43×10^{-3}	30	0–13.3
[5d]	Inductance	Diameter: 3; thickness: 1	0.45	1.36×10^{-3}	Unknown	−1.33–2
[9a]	Inductance	6 × 5 × 0.8	−0.11	-10.72×10^{-3}	Unknown	0–6.67
This work	Inductance	10 × 10 × 2.65	−0.19	-4.3×10^{-3}	35	0–20

[a]Sensitivity has been converted to the values in unit of MHz kPa^{-1}, in which df and dp denote the resonant frequency changes and an applied pressure, respectively; [b]The value represents the relative resonant frequency changes per kilopascal, in which f_0 is the zero-pressure resonant frequency.

To date, diversified research efforts have been devoted to meet the requirements in the developments of soft pressure sensing systems. Appealing performances have been achieved, including high sensitivity (25.1[19] and 47.7 kPa^{-1}[20]), large sensing range (353 kPa[20]), a low limit-of-detection pressure (0.5 Pa[21]), fast response time and low hysteresis (17 ms[22]), additional functionality (strain,[23] torsion and bending measurements,[22] and self-power system[3a]) and detecting specificity (sharpness and location,[24] three-axial force sensing[25]). In comparison, LC-based soft passive sensors feature simple construction and dimensional miniaturization, implantability and no complicated electrical wirings. However, there remain several challenges, such as limitation in detecting distance, usually on the order of a few of centimeters, and signal fluctuations under parasitic noises. Further technical developments of flexible pressure sensors including our next-generation WiPSA should be oriented to address those challenges.

3. Conclusion

A textile-based wireless pressure sensor array for wearable electronics has been developed by utilizing an LC passive sensing scheme. Distinct from the previous reports, our fabric-based WiPSA device integrates ferrite films with an exceptional permeability in a wide frequency range, featuring a robust phase depth in a fully flexible design. We have demonstrated a device sensitivity of as high as of −0.19 MHz kPa^{-1} within the pressure range of 0–20 kPa and a high quality factor of more than 35. The WiPSA device exhibits a great reproducibility in multicycled operations or against temperature/humidity fluctuations or metal interferences. Moreover, our WiPSA device has the advantages of bypassing a solid power source and electrical connection wires, thus presenting a highly portable and wearable format. It has been implemented in several systems for monitoring characteristic human body movements, including a smart wrist band, a footwear insole, and a waist supporter. Our textile-based WiPSA is a promising platform in tactile sensing for a wide range of applications, in particular, for the emerging wearable electronics.

4. Experimental Section

Materials and Methods: The WiPSA device consists of three layers: the ferrite film, the fabric spacer with 3D microstructures, and the passive antenna. The general process of device fabrication includes three steps: antenna fabrication, laser micromachining, and device assembly. In the first step, we patterned a double-sided copper-clad polyimide film using the standard screen printing method and a wet etching process. The capacitors and inductors were formed on the two sides of the film. The two copper layers were connected by though-hole copper plating, followed by lamination of a polyimide film (25 µm thick) with a thin layer of adhesive on each electrode side. In the second step, direct laser micromachining was employed to specify the geometrical shape of the ferrite films (Nanjing Advanced Magnetic Material, Co., Ltd.), the antennas, and the fabric layer (Suzhou Haoke Textile, Co., Ltd.) in one single step. Alignment markers in the fabric spacer were created in this step. In the final assembly, the ferrites films and antennas were aligned to the corresponding positions on the fabric spacer by applying a layer of double-sided adhesive tape (467MP, 3M). The whole device of WiPSA was soft and flexible, with the dimensional size of 10 mm × 10 mm × 2.65 mm for each sensing unit.

Construction of Device Calibration System: A custom-built calibration system was developed to experimentally evaluate the device performance. The system was composed of a linear stage motorized by a step motor with a movement resolution of 0.1 µm (LTS300/M, Thorlabs, Inc.), a force gauge with 10 mN resolution (M5-2, Mark-10, Corp.), and an impedance analyzer (6500B, Wayne Kerr). A desktop computer was used to control the movement of the linear stage, providing a platform to manipulate the mechanical loads and the displacements simultaneously. These parameters were monitored by the force gauge and step motor with feedbacks to the computer. The pressure was determined by the ratio of the force and the area of each sensing unit.

Calibrations on the Mechanical-to-Electrical Sensitivity: A read coil was placed under the sensor with a constant separation distance of 4.5 mm. The phase-frequency spectrum of the read coil was monitored by the impedance analyzer in an analysis mode at an AC excitation voltage of 1 V and a sweeping frequency ranging from up to 60 MHz. The mechanical-to-resonant frequency responses were evaluated twice on two identical sensing units.

Characterizations on the Mechanical Reliability of WiPSAs: A periodic load up to 20 kPa with a frequency of 0.125 Hz was applied to one unit. The output impedances of the coupling coil at 44 MHz were recorded at a sampling frequency of about 4 Hz. The resonant frequency of the sensor was back calculated through a transformer equation.[8c] To characterize the mechanical stability of the device, a commercial electrical driven pin actuator (HongBaoLi Electronic, Co., Ltd.), powered by a pulsed voltage signal at 10 Hz, has been used to apply periodic pressure (20 000 cycles) to the sensor surface.

Characterizations on the Environmental Influences: The devices were placed over a hot plate of which the surface temperature were monitored by an infrared thermometer (i-Quip). The resonant frequencies of the devices were measured through an external coil at various temperature levels. To characterize the humidity influences, the devices were placed in a chamber with an opening, from which the humidity in the chamber can be controlled by a humidifier. The humidity level in the chamber was also monitored by a commercial humidity sensor (AS ONE). To characterize the metal influences, a cylindrical metal block made of stainless steel with a weight of 500 g was placed over the sensor surface with a separation distance of 2 mm. The resonant phase-frequency spectra were recorded by the impedance analyzer.

Supporting Information

Supporting Information is available from the Wiley Online Library or from the author.

Acknowledgements

This work was supported by the National Basic Research Program of China under Grant No. 2014CB748600; the National Natural Science Foundation of China under Grant Nos. 61601317, 81371629, and 61622114; Natural Science Foundation of the Jiangsu Province under Grant No. BK20140052; the 111 project; Collaborative Innovation Center of Suzhou Nano Science and Technology; and the Priority Academic Program Development of Jiangsu Higher Education Institutions (PAPD). The authors also thank Xinran Tang and Taoran Li for their help in drawing the images in this work.

Conflict of Interest

The authors declare no conflict of interest.

Keywords

healthcare monitoring, LC passive resonators, pressure sensor arrays, wearable devices, wireless transmissions

Received: December 11, 2018
Revised: January 26, 2019
Published online: February 21, 2019

[1] a) S.-S. Lee, K.-H. Choi, S.-H. Kim, S.-Y. Lee, *Adv. Funct. Mater.* **2018**, *28*, 1705571; b) J. Lee, S. Shin, S. Lee, J. Song, S. Kang, H. Han, S. Kim, S. Kim, J. Seo, D. Kim, T. Lee, *ACS Nano* **2018**, *12*, 4259; c) X. X. Chen, Y. Song, Z. M. Su, H. T. Chen, X. L. Cheng, J. X. Zhang, M. D. Han, H. X. Zhang, *Nano Energy* **2017**, *38*, 43; d) S. Takamatsu, T. Lonjaret, D. Crisp, J. M. Badier, G. G. Malliaras, E. Ismailova, *Sci. Rep.* **2015**, *5*, 15003; e) M. C. Zhang, C. Y. Wang, H. M. Wang, M. Q. Jian, X. Y. Hao, Y. Y. Zhang, *Adv. Funct. Mater.* **2017**, *27*, 1604795.

[2] a) Y.-C. Lai, J. Deng, S. L. Zhang, S. Niu, H. Guo, Z. L. Wang, *Adv. Funct. Mater.* **2017**, *27*, 1604462; b) Y. Kim, S. Jang, B. J. Kang, J. H. Oh, *Appl. Phys. Lett.* **2017**, *111*, 073502; c) R. Li, Y. Si, Z. Zhu, Y. Guo, Y. Zhang, N. Pan, G. Sun, T. Pan, *Adv. Mater.* **2017**, *29*, 1700253.

[3] a) L. Lin, Y. N. Xie, S. H. Wang, W. Z. Wu, S. M. Niu, X. N. Wen, Z. L. Wang, *ACS Nano* **2013**, *7*, 8266; b) M. M. Liu, X. Pu, C. Y. Jiang, T. Liu, X. Huang, L. B. Chen, C. H. Du, J. M. Sun, W. G. Hu, Z. L. Wang, *Adv. Mater.* **2017**, *29*, 1703700; c) J. Lee, H. Kwon, J. Seo, S. Shin, J. H. Koo, C. Pang, S. Son, J. H. Kim, Y. H. Jang, D. E. Kim, T. Lee, *Adv. Mater.* **2015**, *27*, 2433.

[4] a) S. Han, J. Kim, S. M. Won, Y. J. Ma, D. Kang, Z. Q. Xie, K. T. Lee, H. U. Chung, A. Banks, S. Min, S. Y. Heo, C. R. Davies, J. W. Lee, C. H. Lee, B. H. Kim, K. Li, Y. D. Zhou, C. Wei, X. Feng, Y. G. Huang, J. A. Rogers, *Sci. Transl. Med.* **2018**, *10*, eaan4950; b) M. Singh, N. Jain, *IEEE Sens. J.* **2016**, *16*, 8322; c) S. I. Park, D. S. Brenner, G. Shin, C. D. Morgan, B. A. Copits, H. U. Chung, M. Y. Pullen, K. N. Noh, S. Davidson, S. J. Oh, J. Yoon, K. I. Jang, V. K. Samineni, M. Norman, J. G. Grajales-Reyes, S. K. Vogt, S. S. Sundaram, K. M. Wilson, J. S. Ha, R. Xu, T. Pan, T. I. Kim, Y. Huang, M. C. Montana, J. P. Golden, M. R. Bruchas, R. W. Gereau, J. A. Rogers, *Nat. Biotechnol.* **2015**, *33*, 1280; d) X. Y. Zhang, Z. Zhang, Y. F. Li, C. R. Liu, Y. X. Guo, Y. Lian, *IEEE J. Solid-State Circuits* **2016**, *51*, 3152; e) W. Gao, S. Emaminejad, H. Y. Y. Nyein, S. Challa, K. V. Chen, A. Peck, H. M. Fahad, H. Ota, H. Shiraki, D. Kiriya, D. H. Lien, G. A. Brooks, R. W. Davis, A. Javey, *Nature* **2016**, *529*, 509.

[5] a) W. Deng, L. Wang, L. Dong, Q. Huang, *IEEE Sens. J.* **2018**, *18*, 4886; b) Q. Tan, T. Luo, T. Wei, J. Liu, L. Lin, J. Xiong, *J. Microelectromech. Syst.* **2017**, *26*, 351; c) C. Zhang, L.-F. Wang, J.-Q. Huang, Q.-A. Huang, *J. Microelectromech. Syst.* **2015**, *24*, 575; d) S. H. Song, A. Kim, M. Brown, C. Jung, S. Ko, B. Ziaie, *IEEE Trans. Biomed. Eng.* **2016**, *63*, 2273; e) Y. R. Jeong, J. Kim, Z. Q. Xie, Y. G. Xue, S. M. Won, G. Lee, S. W. Jin, S. Y. Hong, X. Feng, Y. G. Huang, J. A. Rogers, J. S. Ha, *NPG Asia Mater.* **2017**, *9*, e443; f) B. Nie, T. Yao, Y. Zhang, J. Liu, X. Chen, *Appl. Phys. Lett.* **2018**, *112*, 031904.

[6] J. Kim, M. Kim, M. S. Lee, K. Kim, S. Ji, Y. T. Kim, J. Park, K. Na, K. H. Bae, H. K. Kim, F. Bien, C. Y. Lee, J. U. Park, *Nat. Commun.* **2017**, *8*, 14997.

[7] L. Y. Chen, B. C. K. Tee, A. L. Chortos, G. Schwartz, V. Tse, D. J. Lipomi, H. S. P. Wong, M. V. McConnell, Z. A. Bao, *Nat. Commun.* **2014**, *5*, 6028.

[8] a) G. Chitnis, T. Maleki, B. Samuels, L. B. Cantor, B. Ziaie, *IEEE Trans. Biomed. Eng.* **2013**, *60*, 250; b) M. A. Fonseca, M. G. Allen, J. Kroh, J. White, presented at Proc. Tech. Dig. Solid-State Sensor, Actuator, and Microsystems Workshop, Hilton Head Island, SC, June **2006**; c) Q. Huang, L. Dong, L. Wang, *J. Microelectromech. Syst.* **2016**, *25*, 822;

[9] a) C. I. Jang, K. S. Shin, M. J. Kim, K. S. Yun, K. H. Park, J. Y. Kang, S. H. Lee, *Appl. Phys. Lett.* **2016**, *108*, 103701; b) M. Saidani, M. A. M. Gijs, *J. Microelectromech. Syst.* **2003**, *12*, 172.

[10] R. Nopper, R. Niekrawietz, L. Reindl, *IEEE Trans. Instrum. Meas.* **2010**, *59*, 2450.

[11] P. V. Nikitin, K. V. S. Rao, S. Lazar, presented in *2007 Proc. IEEE International Conference on RFID*, Gaylord Texan Resort, Grapevine, TX, March **2007**.

[12] a) H. S. Kim, S. Sivaramakrishnan, S. Sezen, R. Rajamani, *IEEE Sens. J.* **2010**, *10*, 10; b) D. Lei, L.-F. Wang, Q.-A. Huang, *IEEE Sens. J.* **2016**, *16*, 958.

[13] a) X. Miao, M. Ge, *Fibres Text. East. Eur.* **2008**, *16*, 90; b) Y. Liu, H. Hu, L. Zhao, H. Long, *Text. Res. J.* **2012**, *82*, 11.

[14] J. S. Wilson, *Sensor Technology Handbook*, Newnes, Burlington, MA **2005**.

[15] L. Dong, L. Wang, Q. Huang, *IEEE Sens. Lett.* **2018**, *2*, 1.

[16] R. Schuh, H. Trnka, A. Sabo, M. Reichel, K. Kristen, *Arch. Orthop. Trauma Surg.* **2011**, *131*, 197.

[17] T. D. A. Bacarin, I. C. N. Sacco, E. M. Hennig, *Clinics* **2009**, *64*, 113.

[18] P. J. Chen, S. Saati, R. Varma, M. S. Humayun, Y. C. Tai, *J. Microelectromech. Syst.* **2010**, *19*, 721.

[19] Y. Pang, K. N. Zhang, Z. Yang, S. Jiang, Z. Y. Ju, Y. X. Li, X. F. Wang, D. Y. Wang, M. Q. Jian, Y. Y. Zhang, R. R. Liang, H. Tian, Y. Yang, T. L. Ren, *ACS Nano* **2018**, *12*, 2346.

[20] Y. Lee, J. Park, S. Cho, Y. E. Shin, H. Lee, J. Kim, J. Myoung, S. Cho, S. Kang, C. Baig, H. Ko, *ACS Nano* **2018**, *12*, 4045.

[21] Y. P. Zang, F. J. Zhang, D. Z. Huang, X. K. Gao, C. A. Di, D. B. Zhu, *Nat. Commun.* **2015**, *6*, 6269.

[22] S. Gong, W. Schwalb, Y. Wang, Y. Chen, Y. Tang, J. Si, B. Shirinzadeh, W. Cheng, *Nat. Commun.* **2014**, *5*, 3132.

[23] D. J. Lipomi, M. Vosgueritchian, B. C. Tee, S. L. Hellstrom, J. A. Lee, C. H. Fox, Z. Bao, *Nat. Nanotechnol.* **2011**, *6*, 788.

[24] S. Gong, Y. Wang, L. Yap, Y. Ling, Y. Zhao, D. Dong, Q. Shi, Y. Liu, H. Uddin, W. Cheng, *Nanoscale Horiz.* **2018**, *3*, 640.

[25] L. Viry, A. Levi, M. Totaro, A. Mondini, V. Mattoli, B. Mazzolai, L. Beccai, *Adv. Mater.* **2014**, *26*, 2659.